UC Santa Cruz

UC Santa Cruz Previously Published Works

Title

Nanocone-Modified Surface Facilitates Gas Bubble Detachment for High-Rate Alkaline Water Splitting

Permalink

https://escholarship.org/uc/item/1r57h1cx

Journal

Advanced Energy Materials, 13(39)

ISSN

1614-6832

Authors

Ren, Qiu

Feng, Longsheng

Ye, Congwang

et al.

Publication Date

2023-10-01

DOI

10.1002/aenm.202302073

Copyright Information

This work is made available under the terms of a Creative Commons Attribution License, available at https://creativecommons.org/licenses/by/4.0/

Peer reviewed

eScholarship.org Powered by the California Digital Library
University of California

Nanocone-Modified Surface Facilitates Gas Bubble Detachment for High-Rate Alkaline Water Splitting

Qiu Ren,[§] Longsheng Feng,[§] Congwang Ye, Xinzhe Xue, Dun Lin, Samuel Eisenberg, Tianyi Kou, Eric B. Duoss, Cheng Zhu* and Yat Li*

Qiu Ren, Xinzhe Xue, Dun Lin, Samuel Eisenberg and Prof. Yat Li
Department of Chemistry and Biochemistry, University of California, 1156 High Street, Santa Cruz, California 95064, USA
E-mail: yatli@ucsc.edu

Dr. Longsheng Feng, Dr. Congwang Ye, Dr. Eric B. Duoss and Dr. Cheng Zhu
Lawrence Livermore National Laboratory, 7000 East Avenue, Livermore, California 94550, USA
E-mail: zhu6@llnl.gov

Prof. Tianyi Kou
School of Mechanical, Electrical and Information Engineering, Shandong University, Weihai, 264209, P.R. China

*Corresponding authors

[§]These authors contributed equally to this work.

Abstract

The significant amount of gas bubbles generated during high-rate alkaline water splitting (AWS) could be detrimental to the process. The accumulation of bubbles will block the active catalytic sites and hinder the ion and electrolyte diffusion, limiting the maximum current density. Furthermore, the detachment of large bubbles can also damage the electrode's surface layer. Here we demonstrate a general strategy for facilitating bubble detachment by modifying the nickel electrode surface with nickel nanocone nanostructures, which turns the surface into underwater superaerophobic. Simulation and experimental data show that bubbles take a considerably shorter time to detach from the nanocone-modified nickel foil than the unmodified foil. As a result, these bubbles also have a smaller detachment size and less chance for bubble coalescence. The nanocone-modified electrodes, including nickel foil, nickel foam, and 3D-printed nickel lattice, all show substantially reduced overpotentials at 1000 mA cm^{-2} compared to their pristine counterpart. The electrolyzer assembled with two nanocone-modified nickel lattice electrodes retains >95% of the performance after testing at ~900 mA cm^{-2} for 100 hours. The surface NC structure is also well preserved. Our findings offer an exciting and simple strategy for enhancing the bubble detachment and, thus, the electrode activity for high-rate AWS.

Alkaline water splitting (AWS) is one of the most attractive technologies for green hydrogen production.[1] In comparison to the acidic proton exchange membrane (PEM), AWS offers greater flexibility in using non-platinum group metal catalysts and could generate higher-purity hydrogen.[2] However, commercial AWS systems are normally operated at a lower current density (~400 mA cm^{-2}) than PEM electrolyzers.[3] To rapidly generate hydrogen at an industrial scale, it is critical to boosting the operating current density of AWS to a level of ~1000 mA cm^{-2}.[4]

Nevertheless, gas bubbles generation and accumulation on electrodes could limit the current density of high-rate AWS. Bubbles can block the catalysts' active site, hinder electrolyte diffusion, and increase Ohmic resistance, thus deteriorating the reaction rate and restricting the cell voltage efficiency.[5] The detachment of gas bubbles may also damage the catalyst layer. Numerous efforts have been made to actively remove bubbles, including the circulation of electrolytes across the electrode surface[6] and the application of an acoustic and magnetic field.[7] Nevertheless, these approaches require the use of additional instruments and cause extra energy and material costs. Alternatively, the bubble problem can also be tackled by modifying the electrode surface, including fabricating nanostructured catalysts and electrodes,[8] and decorating a superaerophobic polymer layer on electrodes.[9] Furthermore, bubble issues can be addressed by optimizing the AWS device, such as the bubble-free electrolysis concept demonstrated in the capillary-fed electrolysis cell.[10]

The bubble evolution on the electrode surface involves a few steps, including nucleation, growth, detachment, and transport processes.[5a] Our previous work demonstrated that 3D-printed Ni lattice electrodes (3DPNi) with periodic pore structures could mitigate bubble

trapping.[11] The rapid release of bubbles from the ordered structures enhances the accessibility of electrolytes to active sites compared to Ni foam (NF) with tortuous pore structures. As a result, the 3DPNi achieved higher current density than NF at the same potential. Numerous nanostructured surfaces have also been exploited to improve the gas bubble detachment, such as nanostructured MoS_2,[8b] pine-shaped Pt nanoarrays,[12] and WS_2 nanoarrays for HER,[8a] and three-dimensional NiFe layered double hydroxide for OER.[13] Using nanoarray modification strategies, some catalysts with nanostructured surfaces can be operated at high current densities (> 500 mA cm^{-2}), such as nanostructured CoMoSx/NF,[14] nano Ni–Co oxyhydroxide,[15] and graphdiyne/molybdenum oxide nanowall.[16] In this work, we aim to improve the bubble detachment efficiency at ultrahigh current densities (up to 1000 mA cm^{-2}) by modifying the Ni electrode's surface with metallic Ni nanocone (NC) structures. The NCs and the substrate (control sample) are made of the same material and are expected to have similar intrinsic catalytic activity, so the performance variation between the samples is solely due to the surface morphological difference. Our simulation and experimental results confirm that surface modification minimizes the bubble detachment size and time and, thus, effectively reduces the overpotential for HER and OER.

In AWS, the bubble detachment relates to the interaction at the three-phase (solid, liquid, and gas) contact line (TPCL) and is governed by two main forces, the upward buoyant force, and the downward adhesive force.[17] The buoyant force increases with the bubble size, while the adhesive force is closely related to the electrode surface's aerophobicity. A bubble detaches from the electrode when the adhesive force is exceeded by the buoyant force. When the surface roughness is increased, bubbles cannot penetrate the rough surface's recesses, resulting in a

composite interface composed of both solid and liquid phases. This phenomenon can be explained by the Cassie-Baxter model (Equation 1),[18] which investigates the influence of electrode surface roughness on bubble contact angle. As shown in Equation 1, a reduced contact area between the bubble and the rough surface increases the bubble's apparent contact angle,

$$cos\alpha^* = f_s(cos\alpha + 1) - 1 \quad \text{(Equation 1)}$$

where α^* represents the apparent bubble contact angle between a rough surface with liquid, α is the apparent bubble contact angle on a smooth surface, f_s denotes the fraction of the solid in contact with the bubble (**Figure 1**). Compared to a smooth surface, the surface with nanoarchitectures is expected to have a smaller f_s and, therefore, a higher contact angle and aerophobicity.[19] Furthermore, the diameter of the detached bubble (D_d) is also proportional to the sine function of the bubble contact angle, as shown in Equation 2.[17]

$$D_d = \sqrt{\gamma} sin\alpha \sqrt{\frac{6}{\rho g}} \quad \text{(Equation 2)}$$

$\sqrt{\gamma}$ is the surface tension at TPCL, α is the contact angle between the bubble and the solid surface, ρ and g represent the density of the electrolyte and gravitational acceleration, respectively. According to Equation 2, the D_d decreases with the increase of α, which is in the range of 90-180 degrees. A superaerophobic surface has a large air bubble contact angle on an underwater substrate, typically exceeding 150°,[20] can significantly reduce the contact area and adhesive force and, thus, facilitates bubble detachment and reduce the size of bubbles at detachment (**Figures 1a** and **b**).

To validate our hypothesis, we compared the bubble detachment efficiency of a bare Ni foil with a Ni foil surface modified with Ni nanocones (denoted as Foil_NC). We anticipated that the NC-modified surface should have increased roughness and increased apparent bubble

contact angle. NCs were synthesized on a Ni foil using an electrodeposition method reported elsewhere (Experimental Section).[21] The scanning electron microscopy (SEM) image shows that the Ni foil is completely covered with NCs (**Figures 1c** and **d**). NCs have a relatively large size distribution, with the base size typically in the range of 300-700 nm. X-ray powder diffraction (XRD) pattern was collected for the NCs synthesized on carbon paper using the same electrodeposition method and conditions. As shown in Figure S1 (Supporting Information), NCs and Ni foil exhibit a similar set of three major diffraction peaks located at $2\theta = 44.5$, 51.8, and 76.4 degrees, which are well matched with the values reported for Ni (111), (200) and (220) facets, respectively. In addition, we also performed X-ray photoelectron spectroscopy (XPS) analysis on the Ni substrates with and without NC modification. As shown in Figure S2 (Supporting Information), the two samples have similar XPS profiles, exhibiting two broad peaks centered at ~861.4 eV (satellite peak) and ~855.3 eV, respectively. The 855.3 eV peak can be deconvoluted into three sub-peaks. The peak located at 853.3 eV is consistent with the value reported for metallic Ni, while the peaks centered at higher binding energies of 855.2 eV and 856.7 eV correspond to the signals of Ni^{2+} and Ni^{3+}, respectively. The XRD and XPS results together suggest that the NC-modified electrode and bare Ni substrate have similar surface composition and likely similar intrinsic catalytic activity for water splitting. Moreover, contact angle measurements (**Figures 1e** and **f**) revealed that Foil_NC has a considerably larger air contact angle (151.8°) than that of Foil (134.6°). The results are consistent with the theory and confirm the surface NC modification increases the substrate's aerophobicity.

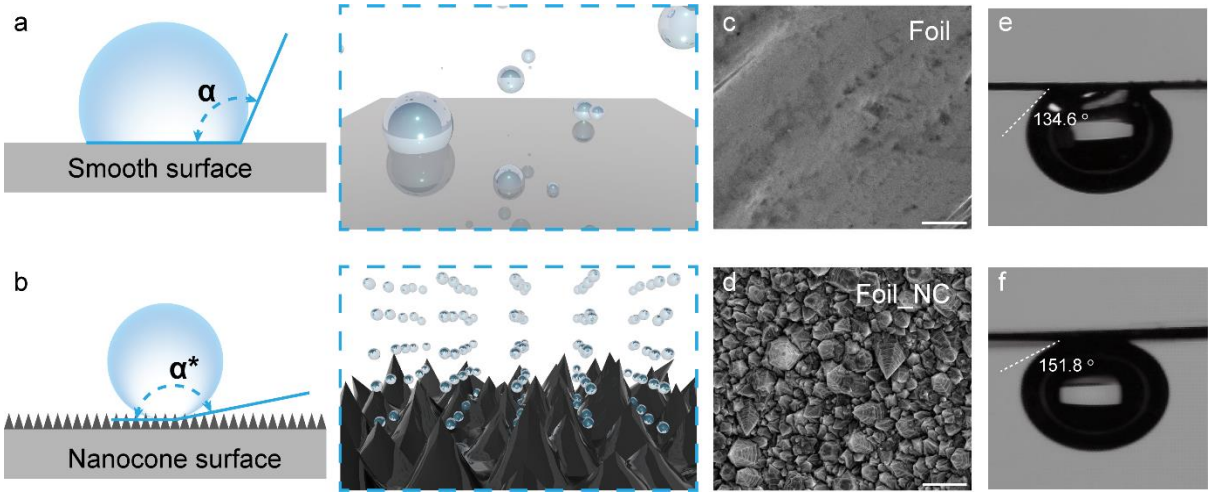

Figure 1. Schematic illustration of bubble contact angle, area and evolution on (a) a smooth and (b) a NC-modified Ni surface. The SEM images of (c) Foil and (d) Foil_NC. Scale bars are 1 μm. Digital images showing the air contact angles on (e) Foil and (f) Foil_NC.

To investigate the influence of electrode surface geometry on bubble detachment, we conducted simulations using a Shan-Chen-type multicomponent multiphase model (for detailed model specifications, refer to the Experiment Section). Specifically, we examined the bubble detachment process on both flat and cone-decorated surfaces. We positioned a single bubble on a substrate featuring either a flat or cone-decorated surface and recorded the attachment time (t_A), which represents the total simulation duration during which the bubble remained in contact with the surface. To manipulate the contact area between the bubble and the cone-decorated surface, we varied the initial depth of the bubble within the surface cones (h/h_0, refer to **Figure 2e** for a schematic illustration of the initial depth). As previously discussed, bubble detachment hinges on the interplay between the buoyancy force and the adhesion force between the bubble and the substrate. Consequently, we employed the

attachment time t_A as a metric to elucidate the impact of distinct surface morphologies and contact areas on the onset of bubble detachment.

Figures 2a-d presents the simulation results for four scenarios: one flat surface and three cone-decorated surfaces with h/h_0 ratios of 1, 2/3, and 1/3. Each subfigure consists of two rows. The first row provides a 3D view of the simulation box, while the second row presents a 2D vertical cross-section of the box to illustrate the substrate shape and the bubble's contour. **Figure 2f** compares the normalized attachment time across these four scenarios. For the flat surface (**Figure 2a**), the bubble remains attached to the substrate throughout the simulation (t*=1), whereas it detaches from all three cone-decorated surfaces (t*=1 in **Figures 2b-d**). Notably, among the cone-decorated surfaces, bubbles with shallower initial depths tend to detach earlier. The detachment onset occurs at 0.35 for $h/h_0 = 1/3$, while the corresponding values increase to 0.46 and 0.65 for $h/h_0 = 2/3$ and $h/h_0 = 1$, respectively. This straightforward analysis clearly demonstrates the benefits of cone-decorated surfaces in facilitating bubble detachment, which can be attributed to two main factors. Firstly, surface cones reduce the contact area between the bubble and the electrode, and as the contact area decreases, the duration of contact between the bubble and the substrate diminishes accordingly. Secondly, since the adhesion force acts perpendicular to the surface normal, it opposes the buoyancy force on a flat surface. In contrast, on a cone-decorated surface, the adhesion force is not directly opposite to the buoyancy force but instead forms an angle (depending on the opening angle of the cone), thereby diminishing the influence of the adhesion force.

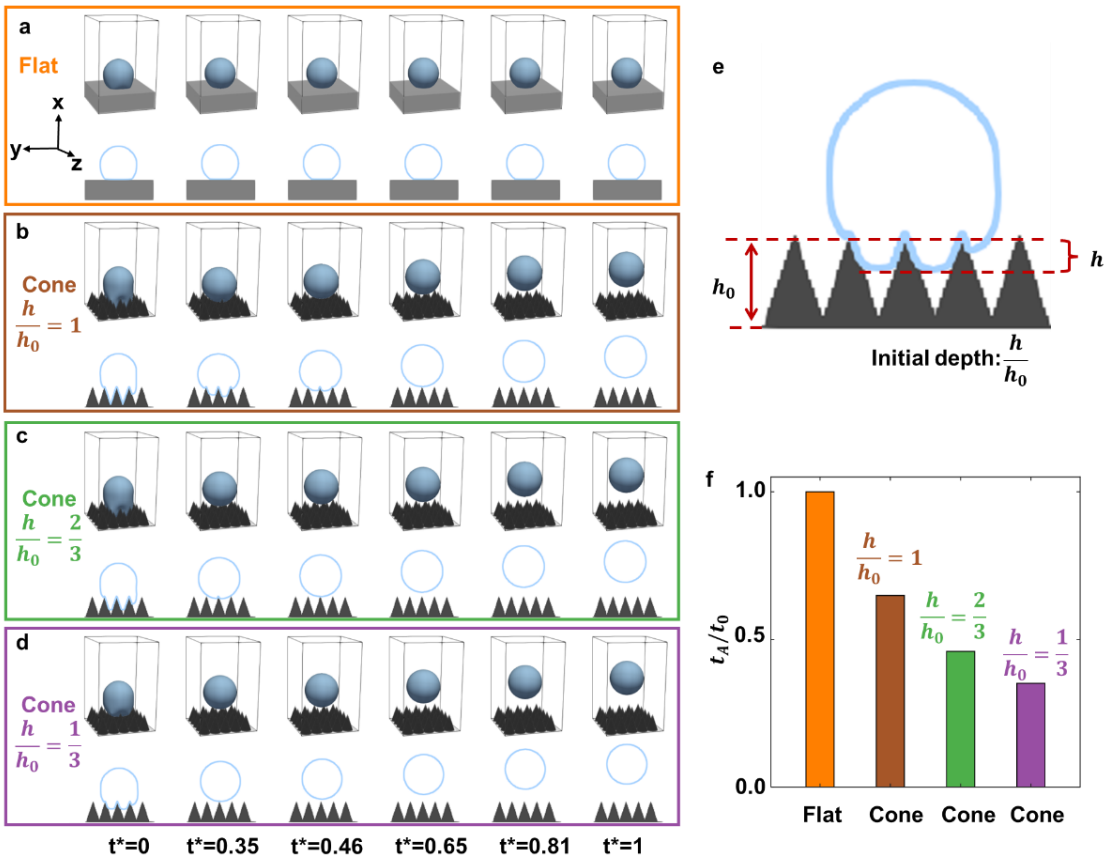

Figure 2. Simulation of a single bubble on a) flat and cone-decorated surfaces with initial depth of b) $h/h_0 = 1$, c) $h/h_0 = 2/3$ and d) $h/h_0 = 1/3$. Normalized simulation time (t*) is labeled for all four cases below d). e) Schematic illustration of the initial depth $\frac{h}{h_0}$. f) Normalized attachment time of the bubble for flat and cone substrates shown a-d.

To experimentally understand the substrate effect on the bubble detachment process, we monitored the bubble evolution on the Foil and Foil_NC samples at fixed current densities using a high-speed camera (Videos S1-4, Supporting Information). **Figures 3a-f** show the bubble evolution on the two substrates at the same hydrogen evolution reaction (HER) current density of 2 mA/cm^2. A single bubble (highlighted by the dashed circle) on each substrate was selected as an example. We set the time (t) when a small bubble appears on the substrate to be zero (t = 0 s). The images show that the bubble grows and eventually detaches from the

substrate. Notably, it takes a significantly shorter time for the bubble to detach from the Foil_NC surface. Moreover, the size of detached bubbles from the Foil_NC surface is also considerably smaller. To exclude the possible effect of non-uniformity on the substrate, we measured more than 100 bubbles detached from different locations on each substrate to obtain the statistical data. The results again confirmed that the bubbles detached from Foil-NC have shorter detachment time (**Figures 3g and h**) and smaller detachment size (**Figures 3i and j**).

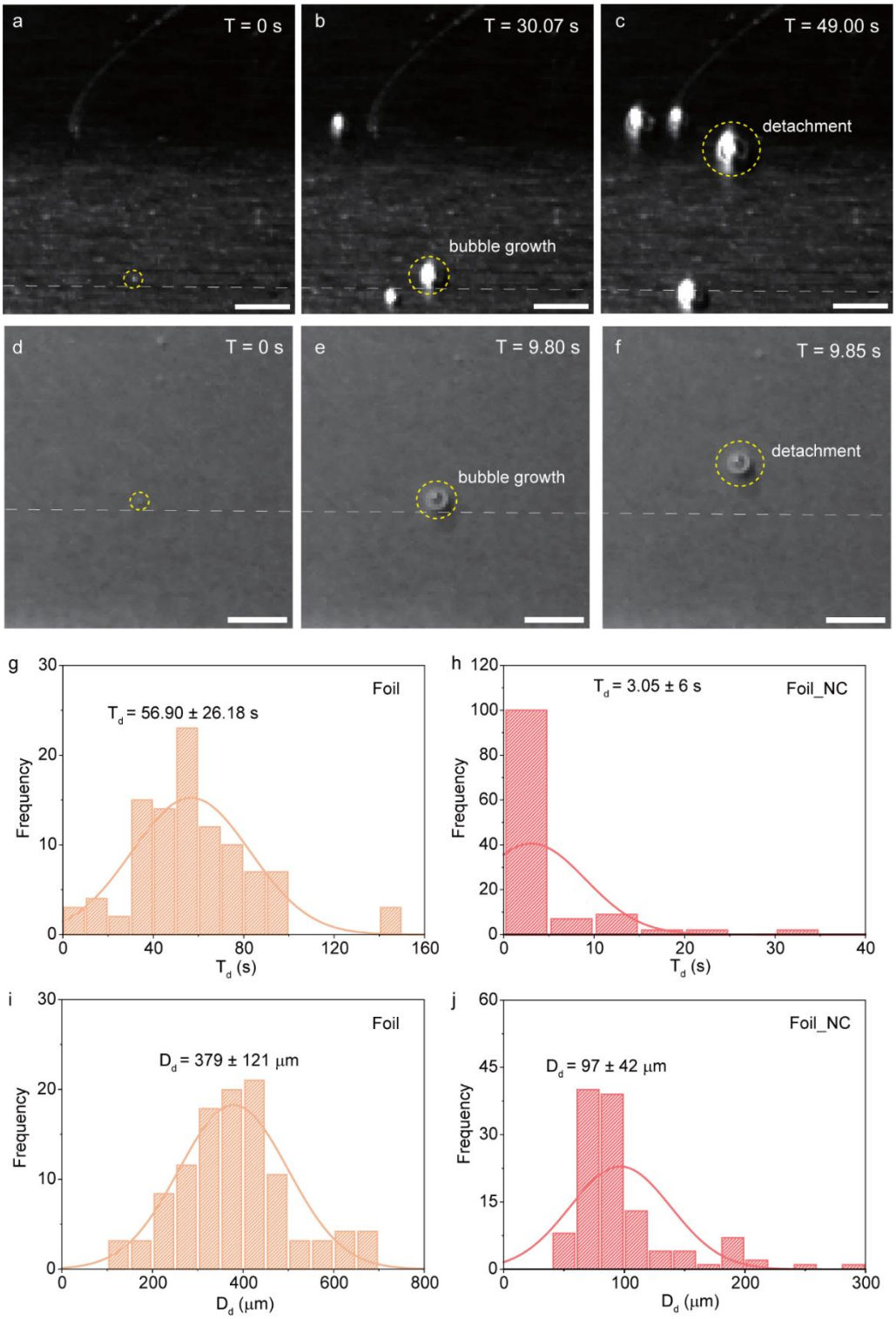

Figure 3. High-speed camera images show the hydrogen bubble evolution process take place on (a-c) Foil and (d-f) Foil_NC, as a function of time. Scale bars are 500 μm. The dashed circles highlight the bubble locations. Histograms illustrate the distribution of (g,h) bubble detachment time (T_d) and (i,j) detachment size (D_d) on Foil and Foil_NC substrates.

We also monitored the gas bubbles evolution in oxygen evolution reaction (OER) at a fixed current density of 4 mA cm^{-2}. The observation agrees well with the HER results; the oxygen gas bubbles detached faster on the Foil_NC substrate with a smaller detachment size (Figure S3, Supporting Information). Interestingly, Figure S3b (Supporting Information) also captures the coalescence process of two nearby gas bubbles which led to a larger size bubble. Bubble coalescence was more frequently observed on Foil than Foil_NC because bubbles have a bigger average size and stay longer on the Foil substrate due to the larger adhesive force.

Furthermore, we also compare the gas bubble evolution on these substrates at fixed voltages. Digital camera images (Figure S4, Supporting Information) and videos (Videos S5-8, Supporting Information) show that more gas bubbles (both oxygen and hydrogen) are generated and released from Foil_NC than those on Foil at the same applied voltages. It suggests that oxygen and hydrogen evolution reactions are more efficient on Foil_NC. To get a quantitative comparison, we measured the HER and OER performances of Foil and Foil_NC in a three-electrode electrochemical cell (Experimental Section). Figures S5a and c (Supporting Information) show the linear sweep voltammograms obtained from the samples in 1.0 M KOH at a scan rate of 0.1 mV s^{-1}. Notably, Foil_NC achieves considerably higher HER and OER current densities than Foil at the same potential. For example, Foil_NC reaches a geometric HER current density (j_{geo}) of 1000 mA cm^{-2} at a potential of -519 mV (vs. RHE), while Foil only has a current density of ~120 mA cm^{-2} at the same potential. Foil requires a potential of -735 mV (vs. RHE) to reach 1000 mA cm^{-2}. The enhanced HER and OER performance of Foil_NC is believed to be due to the rapid bubble detachment that better retains the reaction kinetics and the availability of catalytic sites.

The geometric current density is determined by the intrinsic activity and the total amount of available catalytic active sites.[22] Since both Foil and Foil_NC are metallic Ni and share the same set of Ni crystal facets, they are expected to have similar intrinsic catalytic activity for water splitting. Yet, compared with the Foil sample, the surface NC-modification in Foil_NC increase the electrochemically active surface area (ECSA) largely due to the roughened surface (Figure S6, Supporting Information). When normalizing the current to ECSA, the Foil_NC still exhibits a higher ECSA current density (j_{ECSA}) than that of Foil at the same potential (Figures S5b and d, Supporting Information). The results suggested that the enhanced current density of Foil_NC at high-rate water splitting is related to the rapid detachment of gas bubbles.

We also compare the gas bubble generations from Foil and Foil_NC at the same current density of 1000 mA cm^{-2}. At such a high current, large amounts of gas bubbles are forced to be generated at both electrodes. As shown in Figure S7 and Movie S9-12 (Supporting Information), gas bubble detachment on Foil_NC is smoother and has fewer large bubbles accumulated on the substrate. The results again prove that the NC-modified surface facilitates bubble detachment and is more favorable for high-rate AWS.

In addition to gas bubble evolution behaviors, the bubble transport and releasing from 3D electrodes are equally important for the AWS performance. Our previous studies demonstrated that 3D-printed lattice structures with periodic pores/channels mitigate bubble transport at high-rate conditions.[11, 23] The low tortuosity design minimizes the bubble transport resistance and time by reducing their lateral movements and collisions with the electrode scaffold. Therefore, we extended the concept of NC-modification from 2D foil to 3D structures,

including Ni foam and 3D-printed Ni lattice. NCs were synthesized on these 3D structures using the same electrodeposition method. Although the NC size varies with the growth substrate, both samples have excellent NC coverage (Figures S8 and S9, Supporting Information). The samples (Foam and Lattice) after NC modification are denoted as Foam_NC and Lattice_NC respectively. HER and OER measurements were performed to investigate the effect of NC-modification on Foam_NC (Figure S10, Supporting Information) and Lattice_NC (**Figures 4a-d**). Significantly, the 3D substrates with NC-modified surface exhibit substantially higher j_{geo} and j_{ECSA} than the pristine samples, which is consistent with the results obtained from Ni foil. The results suggest that surface NC-modification to promote gas bubble detachment is a general strategy that can be applied to different substrates. We also compared the HER and OER overpotentials for different NC-modified substrates in order to understand the effect of electrode architecture. As shown in **Figures 4e** and **4f**, the Foam_NC electrode has lower overpotentials than Foil_NC, while the Lattice_NC electrode has the smallest overpotentials among the samples at all the current densities (up to 1000 mA cm^{-2}) we studied. Assuming the NC-modified surfaces on different substrates have a similar structural effect on bubble detachment; we believe the enhanced performance of Lattice_NC electrode is because of the increased active surface area (Figures S11 and 12, Supporting Information). The low-tortuosity lattice structure also allows more rapid bubble transport and releasing compared to Foam_NC, better retaining the active sites for water splitting at high current densities.[11, 24]

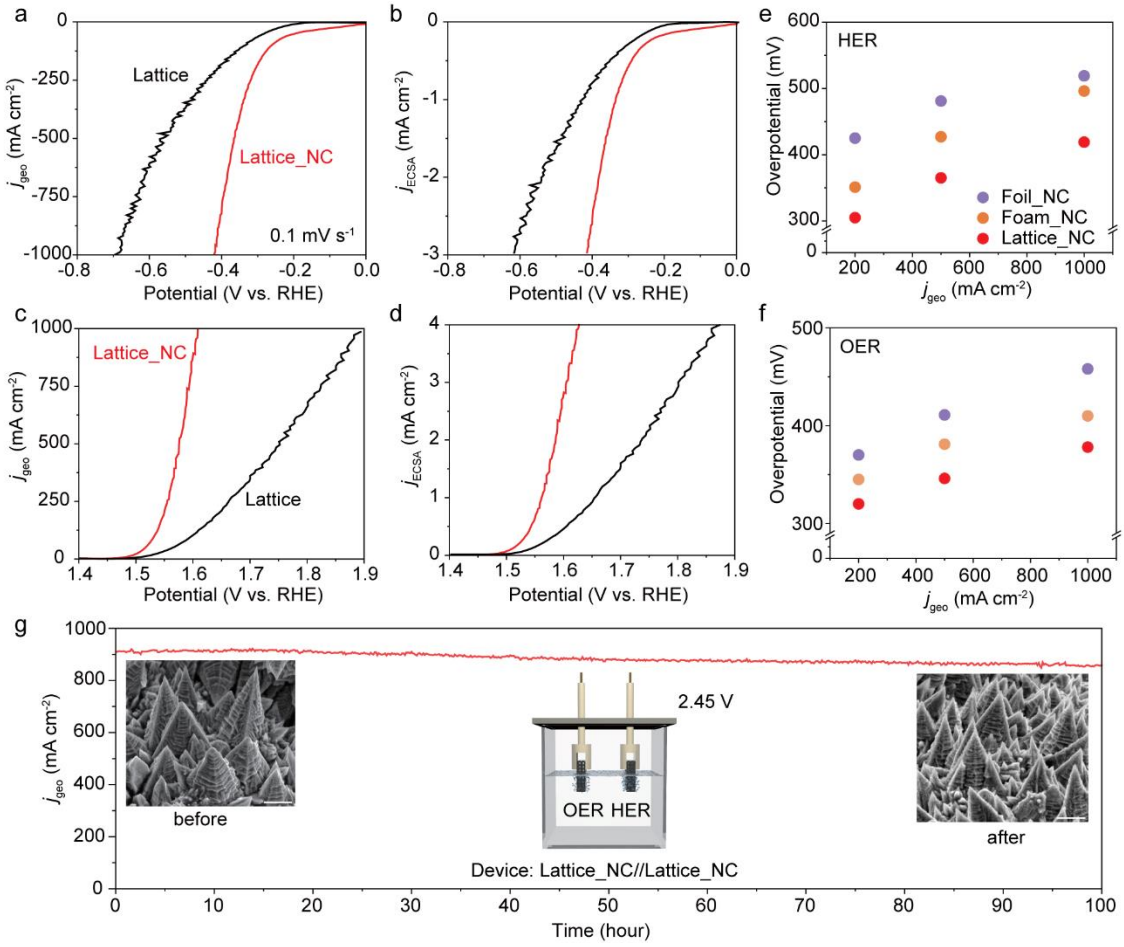

Figure 4. Linear sweep voltammograms of Lattice and Lattice_NC electrodes collected in 1.0 M KOH at a scan rate of 0.1 mV s^{-1} for (a, b) HER and (c,d) OER. Figures (a and c) are plotted in geometric current density, while Figures (b and d) are plotted in ECSA normalized current density. Figures (e and f) compare the HER and OER overpotentials of Foil_NC, Foam_NC, and Lattice_NC at different geometric current densities. (g) The geometric current density of a device assembled with two Lattice_NC electrodes recorded at a fixed voltage of 2.45 V for 100 hours. The inset figure shows a schematic illustration of the two-electrode device. The SEM images show the NC morphology before and after the stability test.

The electrode's electrochemical and mechanical stability are critical factors for determining the practical feasibility of electrolyzers. During high-rate water splitting, the rapid detachment of large amounts of gas bubbles could be detrimental to the deposited catalyst layer. Therefore, we performed a long-term stability test on an AWS device assembled with two Lattice_NC electrodes (**Figure 3g**, inset) in 1.0 M KOH at room temperature. At a fixed applied voltage of 2.45V, the device reached an initial current density of 910 mA cm^{-2}. As shown in **Figure 3g**, the device retains ~95% of the initial current after testing for 100 hours, demonstrating extraordinary electrochemical stability at ultrahigh current density. The SEM images of Lattice_NC collected before and after the stability test under HER conditions confirm that the NC morphology is well maintained (**Figure 3g**, inset). Besides, XPS analysis revealed that Lattice_NC before and after the stability test have similar spectroscopic profiles, still containing deconvoluted peaks corresponding to metal Ni, Ni^{2+}, and Ni^{3+} (Figure S13a, Supporting Information). On the other hand, only Ni^{2+} and Ni^{3+} signals were observed for the Lattice_NC sample after the OER stability test (Figure S13b, Supporting Information). We believe the disappearance of the metallic Ni signal is due to Ni oxidation during OER. Overall, the two main broad peaks in the Ni 2p XPS spectra are retained after the stability test. The XPS results together with the SEM analysis consistently support the outstanding electrochemical and mechanical stability of the NC-modified electrodes, making this surface-modification strategy even more attractive for practical AWS applications.

In summary, we have demonstrated a general strategy to facilitate gas bubble detachment from AWS electrodes by modifying the electrode surface with NC structures. The NC-modified surface shows superaerophobicity. The simulation data indicated the NC-

modified surface can enhance bubble detachment by reducing the contact area between bubble and electrode and diminishing the impact of adhesion force by altering the surface normal of the electrode, rendering it non-parallel to the buoyancy force. The high-speed camera studies confirmed that the bubble detachment size and time on NC-modified electrodes are considerably smaller than that on their pristine counterparts. Consistently, the NC-modified electrodes achieved ultrahigh current density (e.g., 1000 mA cm^{-2}) at substantially lower overpotential than unmodified electrodes, as a result of facilitated gas bubble detachment. In addition, the NC-modified electrodes also showed outstanding electrochemical and mechanical stability. A device assembled with NC-modified 3D-printed lattice electrodes retained >95% of the performance after 100-hours of testing for direct water splitting at room temperature at 2.45 V. The findings offer critical insights into designing nanostructured surfaces for mitigating bubble accumulation issues during high-rate AWS. This surface modification method can also be readily coupled with different electrode and device designs. The capability of increasing the electrode's underwater superaerophobilicity to reduce the bubble's adhesive force could be useful under various conditions such as low-gravity environments.

Experimental section

Ni Ink Preparation

Nickel powder (mean particle size 3-7 micrometer, Alfa Aesar), polylactic-co-glycolic acid copolymer (PLGA, 85:15 PLA:PLG by mass, Sigma-Aldrich), dichloromethane (DCM, b.p. 40 ºC, Sigma-Aldrich), and ethylene glycol butyl ether (EGBE, b.p. 171 ºC, Sigma-Aldrich) were used as received. Typically, 2 g PLGA pellets were fully dissolved into 2 g DCM to

generate a polymeric solution. Then, 26.7 g Ni powders were mixed with this solution to form a colloidal suspension for 30 s at 2000 rpm using a planetary mixer (ARE-250, Thinky). High-speed mixing concentrates the suspension due to the evaporation of DCM. Finally, 1 g EGBE and an appropriate amount of DCM were added to yield a composite ink composed of a total solid loading of 40 vol% and 50 vol% (Ni+PLGA) and balanced DCM:EGBE ratio of 2:1.

Ink Rheology

The rheological properties of the Ni ink were characterized using a stress-controlled Rheometer (AR 2000ex, TA) with a 40-mm-flat plate geometry and a gap of 500 μm in the presence of a solvent trap to avoid solvent evaporation. A stress sweep from 10^{-2} to 10^{3} Pa at a constant frequency of 1 Hz was conducted to record the shear modulus variations as a function of sweep stress. The yield stress (τ_y) was defined as the stress where the storage modulus falls to 90% of the plateau value. A strain sweep from 10^{-1} to 10^{2} s^{-1} was performed to record the apparent viscosities at varying shear rates.

3D Printing of Ni Lattices

The as-prepared Ni inks are loaded into a 10 ml syringe barrel (Nordson EFD) attached by a Luer-Lok to a smooth-flow tapered nozzle [inner diameter (d), 200 μm. An air-powered fluid dispenser (Ultimus V, Nordson EFD) provided the appropriate pressure to extrude the ink through the nozzle. The target patterns were printed using a three-axis positioning stage (ABL9000, Aerotech). The 3D Ni green parts were printed onto a silicon wafer with an initial nozzle height of 0.7 d to ensure adhesion to the substrate. The required pressure depends on the ink rheology, nozzle size, and printing speed, and typical values range from 60 to 90 psi at 5-15 mm s^{-1}. The printed parts were dried in the air and then thermally treated at 300 °C for 1

h and 600 °C for 1 h in H_2. Finally, the samples were heat treated at 900 °C for 3 h in Ar. The typical printed sample *xyz* dimensions were 10 mm × 10 mm × 3 mm, and the linear shrinkage is below 10%.

Syntheses of Ni nanocone on different Ni substrates:

Ni nanocones were synthesized on different Ni substrates (foil, foam and 3D-printed lattice) by an electrodeposition method in a three-electrode system.[21] Specifically, a piece of Ni substrate (1×1 cm) was used as the working electrode, Ag/AgCl was adopted as the reference electrode, and a Ni foam (2×3 cm) was used as the counter electrode. Before electrodeposition, the Ni substrate was pretreated by the following procedure: Ni substrate was cut into a small piece (1×1 cm), and ultrasonicated in acetone, 3 M HCl, DI water and ethanol for 10 min, respectively, then it was dried at ambient conditions. The electrodeposition solution composed of 0.84 M $NiCl_2{\cdot}6H_2O$, 1 M H_3BO_3 and 1.4 M NH_4Cl in 30 mL DI water, and the pH of the solution was adjusted to 4 by using 10% wt NaOH solution. The electrodeposition was performed at a fixed current density of 20 mA cm^{-2} for 8 min at 60 °C. The as-prepared nanocone-modified Ni substrates (Foil_NC, Foam_NC, and Lattice_NC) were thoroughly washed with DI water and ethanol, then dried at ambient conditions.

Air contact angle measurement

The Foil or Foil_NC sample was horizontally suspended in the beaker containing 30 mL of water using a platinum clip. Then, an air bubble with controlled size was carefully injected into the solution and stabilized at the bottom of the sample. The air-solid contact photographs were then captured using an Ossila Contact Angle Goniometer instrument. The acquired images were

analyzed and processed using the Ossila Contact Angle v4.0.0.0 to determine the air contact angle.

Structural Characterization

The morphologies of samples were characterized by SEM (Hitachi S-4800 II). The phase composition of the as-prepared materials was investigated by X-ray diffraction (Rigaku SmartLab). XPS spectra were collected by using Kratos Analytical AXIS Ultra Delay-Line Detector (DLD) instrument.

Simulation

A Shan-Chen-type multiphase multi-component lattice Boltzmann method was employed to investigate the influence of substrate surface on the detachment dynamics of a single bubble. The simulations were conducted utilizing the open-source package Palabos.[25] The Shan-Chen-type model offers an efficient and effective approach for studying complex multiphase flow phenomena, circumventing the need to directly solve the Navier-Stokes equations. The model represents molecular interactions at the mesoscale through a pseudopotential, characterized by local density distributions $f^{\sigma}(\mathbf{r}, t)$), where σ distinguishes between gas and liquid phases, and $\mathbf{r}$ denotes spatial coordinates. Additionally, the model incorporates fluid-fluid interactions $F_{c,\sigma}$, fluid-solid adhesion $F_{ads,\sigma}$, and gravitational force F_g, enabling a comprehensive analysis of the bubble-liquid-substrate system. The model parameters employed in the simulations were selected based on established values.[11] The model was used to perform simulations for both flat and cone-decorated surfaces. The simulation domain was defined with dimensions of 150×100×100, while the substrate was assigned a thickness of 30 units in the x-direction (vertical). For surfaces with cone decorations, the cone geometry was set with a base

radius of 10 units and a height of 30 units. The input parameters for the Shan-Chen-type multiphase multicomponent lattice Boltzmann model used in this work are listed in Table S1 (Supporting Information).

Imaging of bubble evolution

Videos and images were recorded using a high-speed camera (Photron NOVA S9) capable of video capturing at up to 900,000 fps coupled with a macro lens (Nikon 200mm f/4D ED-IF AF Micro Nikkor Lens). It was operated at the frame rate of 60 fps with a shutter speed of 1 ms to visualize the whole gas bubble evolution at low current densities (2 mA cm^{-2} for HER and 4 mA cm^{-2} for OER). The measurement was performed in a three-electrode system with Foil or Foil_NC electrodes (1×1 cm) serving as the working electrode, Hg/HgO and graphite rods were used as reference and counter electrodes, respectively. The three electrodes were submerged in 1.0 M KOH solution inside a transparent container with flat walls to minimize distortion of video capturing. The high-speed camera was mounted aside with an appropriate angle for recording. Because of the small depth of field of the camera lens, the surface of the electrode observed was adjusted to be perpendicular to the camera's viewing angle to keep everything in focus. LED lamps were used around the container to illuminate electrodes and bubbles during the experiment.

Electrochemical measurements

Electrochemical measurements were carried out on the CHI 660D electrochemical workstation in a three-electrode system in 1.0 M KOH solution. Foil_NC, Foam_NC or Lattice_NC served as the working electrode; carbon rod was selected as the counter electrode, and Hg/HgO was used as the reference electrode. For HER, cyclic voltammetry (CV) was first performed in a

potential window of -0.6 to -1.35 V versus Hg/HgO for 50 cycles at a scan rate of 20 mV $s^{-1,}$ and then linear scan voltammograms (LSVs) were collected at 0.1 mV s^{-1} in N_2-saturated electrolyte. For OER, CV was also performed in a potential window of 0 to 0.8 V versus Hg/HgO for 20 cycles at the scan rate of 20 mV s^{-1}. Linear scan voltammograms (LSVs) were then collected at 0.1 mV s^{-1} in O_2-saturated electrolyte. Electrochemical impedance spectroscopy (EIS) was performed at -1.08 V versus Hg/HgO for HER and 0.7 V versus Hg/HgO for OER, with a frequency ranging from 100 kHz to 1 Hz and an amplitude of 5 mV. The R_s (solution resistance) obtained from the electrochemical impedance spectra (Figure S14, Supporting Information) was used for iR compensation. An 85% level of compensation was chosen.[26] The water splitting test was performed at room temperature in a two-electrode configuration using Lattice_NC as both HER and OER electrodes at 2.45 V. The electrochemical active surface area (ECSA) was determined by measuring the capacitive current associated with double-layer charging from the scan-rate dependence of CVs (Supporting Information).

Supporting Information

Supporting Information is available from the Wiley Online Library or from the author.

Acknowledgements

Y.L. thanks the funding support from the faculty research grant from the University of California, Santa Cruz. This work was performed (L.F.) under the auspices of the U.S. Department of Energy by Lawrence Livermore National Laboratory under Contract No. DE-

AC52-07NA27344. IM release number: 1077130. L.F. would also like to acknowledge Dr. Tae Wook Heo from LLNL for many useful discussions on simulation results. The authors thank Dr. Tom Yuzvinsky from the University of California, Santa Cruz for SEM images acquisition, and acknowledge the W. M. Keck Center for Nanoscale Optofluidics for use of the FEI Quanta 3D Dual-beam SEM.

References

[1] a) T. Kou, S. Wang, Y. Li, *ACS Mater. Lett.* **2021**, 3, 224; b) W. Wang, X. Xu, W. Zhou, Z. Shao, *Adv. Sci. (Weinh)* **2017**, 4, 1600371; c) C. Tang, Y. Zheng, M. Jaroniec, S. Z. Qiao, *Angew. Chem. Int. Ed. Engl.* **2021**, 60, 19572; d) M. Chen, T. J. Smart, S. Wang, T. Kou, D. Lin, Y. Ping, Y. Li, *J. Mater. Chem. A* **2020**, 8, 8783; e) T. Kou, M. Chen, F. Wu, T. J. Smart, S. Wang, Y. Wu, Y. Zhang, S. Li, S. Lall, Z. Zhang, Y. S. Liu, J. Guo, G. Wang, Y. Ping, Y. Li, *Nat. Commun.* **2020**, 11, 590.

[2] a) H. Sun, Z. Yan, F. Liu, W. Xu, F. Cheng, J. Chen, *Adv Mater* **2020**, 32, e1806326; b) M. Carmo, D. L. Fritz, J. Mergel, D. Stolten, *Int. J. Hydrogen Energy* **2013**, 38, 4901.

[3] Z. Y. Yu, Y. Duan, X. Y. Feng, X. Yu, M. R. Gao, S. H. Yu, *Adv. Mater.* **2021**, 33, 2007100.

[4] a) Y. Luo, Z. Zhang, M. Chhowalla, B. Liu, *Adv. Mater.* **2022**, 34, 2108133; b) C. Zhang, Y. Luo, J. Tan, Q. Yu, F. Yang, Z. Zhang, L. Yang, H. M. Cheng, B. Liu, *Nat. Commun.* **2020**, 11, 3724; c) X. Zhang, M. Jin, F. Jia, J. Huang, A. Amini, S. Song, H. Yi, C. Cheng, *Energy Environ. Mater.* **2022**, 0, e12457.

[5] a) A. Angulo, P. van der Linde, H. Gardeniers, M. Modestino, D. Fernández Rivas, *Joule* **2020**, 4, 555; b) J. Wang, F. Xu, H. Jin, Y. Chen, Y. Wang, *Adv. Mater.* **2017**, 29, 1605838.

[6] A. Buttler, H. Spliethoff, *Renewable Sustainable Energy Rev.* **2018**, 82, 2440.

[7] a) C. Niether, S. Faure, A. Bordet, J. Deseure, M. Chatenet, J. Carrey, B. Chaudret, A. Rouet, *Nat. Energy* **2018**, 3, 476; b) M. H. Islam, O. S. Burheim, B. G. Pollet, *Ultrason. Sonochem.* **2019**, 51, 533; c) D. Fernández, Z. Diao, P. Dunne, J. M. D. Coey, *Electrochim. Acta* **2010**, 55, 8664.

[8] a) L. Xie, L. Wang, W. Zhao, S. Liu, W. Huang, Q. Zhao, *Nat. Commun.* **2021**, 12, 5070; b) Z. Lu, W. Zhu, X. Yu, H. Zhang, Y. Li, X. Sun, X. Wang, H. Wang, J. Wang, J. Luo, X. Lei, L. Jiang, *Adv. Mater.* **2014**, 26, 2683.

[9] M. Bae, Y. Kang, D. W. Lee, D. Jeon, J. Ryu, *Adv. Energy Mater.* **2022**, 12, 2201452.

[10] A. Hodges, A. L. Hoang, G. Tsekouras, K. Wagner, C. Y. Lee, G. F. Swiegers, G. G. Wallace, *Nat. Commun.* **2022**, 13, 1304.

[11] T. Kou, S. Wang, R. Shi, T. Zhang, S. Chiovoloni, J. Q. Lu, W. Chen, M. A. Worsley, B. C. Wood, S. E. Baker, E. B. Duoss, R. Wu, C. Zhu, Y. Li, *Adv. Energy Mater.* **2020**, 10, 2002955

[12] Y. Li, H. Zhang, T. Xu, Z. Lu, X. Wu, P. Wan, X. Sun, L. Jiang, *Adv. Funct. Mater.* **2015**, 25, 1737.

[13] Z. Lu, W. Xu, W. Zhu, Q. Yang, X. Lei, J. Liu, Y. Li, X. Sun, X. Duan, *Chem. Commun. (Camb)* **2014**, 50, 6479.

[14] X. Shan, J. Liu, H. Mu, Y. Xiao, B. Mei, W. Liu, G. Lin, Z. Jiang, L. Wen, L. Jiang, *Angew. Chem. Int. Ed. Engl.* **2020**, 59, 1659.

[15] J. Abed, S. Ahmadi, L. Laverdure, A. Abdellah, C. P. O'Brien, K. Cole, P. Sobrinho, D. Sinton, D. Higgins, N. J. Mosey, S. J. Thorpe, E. H. Sargent, *Adv. Mater.* **2021**, 33, e2103812.

[16] Y. Yao, Y. Zhu, C. Pan, C. Wang, S. Hu, W. Xiao, X. Chi, Y. Fang, J. Yang, H. Deng, S. Xiao, J. Li, Z. Luo, Y. Guo, *J. Am. Chem. Soc.* **2021**, 143, 8720.

[17] W. Xu, Z. Lu, X. Sun, L. Jiang, X. Duan, *Acc. Chem. Res.* **2018**, 51, 1590.

[18] J. E. George, S. Chidangil, S. D. George, *Adv. Mater. Interfaces* **2017**, 4, 1601088.

[19] B. Su, Y. Tian, L. Jiang, *J. Am. Chem. Soc.* **2016**, 138, 1727.

[20] D. Zhou, P. Li, X. Lin, A. McKinley, Y. Kuang, W. Liu, W. F. Lin, X. Sun, X. Duan, *Chem. Soc. Rev.* **2021**, 50, 8790.

[21] Z. Su, C. Yang, B. Xie, Z. Lin, Z. Zhang, J. Liu, B. Li, F. Kang, C. P. Wong, *Energy Environ. Sci.* **2014**, 7, 2652.

[22] J. Kibsgaard, C. Tsai, K. Chan, J. D. Benck, J. K. Nørskov, F. Abild-Pedersen, T. F. Jaramillo, *Energy Environ. Sci.* **2015**, 8, 3022.

[23] X. Xue, D. Lin, Y. Li, *Small Struct.* **2022**, 3, 2200159.

[24] F. Rocha, R. Delmelle, C. Georgiadis, J. Proost, *Adv. Energy Mater.* **2022**, 13, 2203087.

[25] a) J. Latt, O. Malaspinas, D. Kontaxakis, A. Parmigiani, D. Lagrava, F. Brogi, M. B. Belgacem, Y. Thorimbert, S. Leclaire, S. Li, F. Marson, J. Lemus, C. Kotsalos, R. Conradin, C. Coreixas, R. Petkantchin, F. Raynaud, J. Beny, B. Chopard, *Comput. Math. with Appl.* **2021**, 81, 334. b) J. E. Santos, A. Bihani, C. J. Landry, Git code **2019**, https://doi.org/10.5281/zenodo.5203295.

[26] L. Yu, Z. Ren, *Mater. Today Phys.* **2020**, 14, 100253.